

1 FROM SERPENTINIZATION TO CARBONATION: NEW INSIGHTS FROM A CO₂
2 INJECTION EXPERIMENT

3

4 Frieder Klein^{1*} & Thomas M. McCollom²

5 ^{1*} Department of Marine Chemistry and Geochemistry, Woods Hole Oceanographic
6 Institution, Woods Hole, MA 02543, USA

7 ² Laboratory for Atmospheric and Space Physics, Campus Box 600, University of
8 Colorado, Boulder, CO 80309-0600, USA

9

10 * Corresponding author Tel: +1-508-289-3355, fax: +1-508-289-2183, e-mail:
11 fklein@whoi.edu

12 **Abstract**

13 We injected a CO₂-rich hydrous fluid of seawater chlorinity into an ongoing,
14 mildly reducing (H_{2(aq)} ≈ 3 mmol/kg) serpentinization experiment at 230 °C and 35
15 MPa to examine the changes in fluid chemistry and mineralogy during mineral
16 carbonation. The chemistry of 11 fluid samples was measured, speciated, and
17 compared with MgO-SiO₂-H₂O-CO₂ (MSHC) phase equilibria to approximate the
18 reaction pathway from serpentinization to carbonation. Although the overall system
19 was in apparent disequilibrium, the speciated activities of dissolved silica (aSiO_{2(aq)})
20 and carbon dioxide (aCO_{2(aq)}) evolved roughly along MSHC equilibrium phase
21 boundaries, indicative of 4 distinct mineral assemblages over time: 1) serpentine-
22 brucite (± magnesite) before the injection, to 2) serpentine-talc-magnesite 2 hours
23 after the injection, to 3) quartz-magnesite (48h after injection), and 4) metastable

24 olivine – magnesite (623h after injection) until the experiment was terminated.
25 Inspection of the solid reaction products revealed the presence of serpentine,
26 magnesite, minor talc, and magnetite, in addition to relict olivine. Although quartz
27 was saturated over a short segment of the experiment, it was not found in the solid
28 reaction products. A marked and rapid change in fluid chemistry suggests that
29 serpentinization ceased and precipitation of magnesite initiated immediately after
30 the injection. A sharp decrease in pH after the injection promoted the dissolution of
31 brucite and olivine, which liberated $\text{SiO}_{2(aq)}$ and dissolved Mg. Dissolved Mg was
32 efficiently removed from the solution via magnesite precipitation, whereas the
33 formation of talc was relatively sluggish. This process accounts for an increase in
34 $a\text{SiO}_{2(aq)}$ to quartz saturation shortly after the injection of the CO_2 -rich fluid.
35 Molecular dihydrogen ($\text{H}_{2(aq)}$) was generated during serpentinization of olivine by
36 oxidation of ferrous iron before the injection; however, no additional $\text{H}_{2(aq)}$ was
37 generated after the injection. Speciation calculations suggest a strong affinity for the
38 formation of methane ($\text{CH}_{4(aq)}$) at the expense of $\text{CO}_{2(aq)}$ and $\text{H}_{2(aq)}$ after the
39 injection, but increased $\text{CH}_{4(aq)}$ formation was not observed. These findings suggest
40 that kinetically fast mineral carbonation dominates over sluggish $\text{CH}_{4(aq)}$ formation
41 in mildly reducing serpentinization systems affected by injection of CO_2 -rich fluids.

42

43 **Keywords:** serpentinization; methane formation; mineral carbonation; carbon
44 sequestration; hydrothermal injection experiment

45

46 **1. INTRODUCTION**

47 Mantle rocks have been exposed in a variety of geotectonic settings at the
48 Earth's surface, including ophiolites, alpine orogens, mid-ocean ridges, continental
49 rifted margins, and in fore-arc settings of subduction zones (Cannat et al., 2010;
50 Chidester and Cady, 1972; Coleman, 1977; Dick et al., 2003; Fryer et al., 2006;
51 Whitmarsh et al., 2001). Likewise, hydrous fluids enriched in CO₂ via magmatic
52 degassing, leaching of carbon-bearing rocks, metamorphic decarbonation of marine
53 sediments, or decomposition of organic material occur in many geotectonic settings
54 worldwide (Irwin and Barnes, 1980; Von Damm, 1995). Where mantle rocks and
55 CO₂-rich fluids interact carbonate deposits can form (e.g., Chidester and Cady, 1972;
56 Griffis, 1972; Hansen et al., 2005; Kelemen and Matter, 2008). This process, referred
57 to as mineral carbonation, has received considerable attention as a potential
58 pathway to mitigate emissions of anthropogenic CO₂ (Andreani et al., 2009; Bearat
59 et al., 2006; Boschi et al., 2009; Cipolli et al., 2004; Dufaud et al., 2009; Giammar et
60 al., 2005; Hövelmann et al., 2011; IPCC, 2005; Kelemen et al., 2011; Kelemen and
61 Matter, 2008; Wolf et al., 2003; Zhao et al., 2010). However, the formation of
62 carbonate minerals competes with the reduction of CO₂ under reducing conditions,
63 which develop when ultramafic rocks undergo serpentinization. Experimental
64 studies have demonstrated that dissolved CO₂ present in hydrothermal fluids can be
65 reduced to methane and other hydrocarbons (Foustoukos and Seyfried, 2004;
66 Horita and Berndt, 1999; McCollom and Seewald, 2001), but reaction rates are
67 sluggish unless the reduction is facilitated by effective surface catalysts such as
68 awaruite (Ni₃Fe), a trace mineral common in serpentinite. Indeed, methane
69 emanations have been reported from a number of serpentinization systems on land

70 and at the seafloor (Abrajano et al., 1988; Charlou et al., 2002; Proskurowski et al.,
71 2008). The mechanisms that drive mineral carbonation of ultramafic rocks have
72 been a subject of study by petrologists for at least the past 8 decades (Frost, 1985;
73 Greenwood, 1967; Hansen et al., 2005; Hess, 1933; Koons, 1981; Korzhinskii, 1959;
74 Schandl and Naldrett, 1992; Trommsdorff and Evans, 1977). Supported by
75 thermodynamic reaction path models (Klein and Garrido, 2011), field evidence
76 suggests that serpentinization of ultramafic rocks pre-dates carbonation and
77 changes in secondary mineralogy imply that the chemistry of interacting fluids must
78 change substantially during the alteration process (Frost, 1985; Griffis, 1972; Hess,
79 1933; Weir and Kerrick, 1987). The mineralogical changes during serpentinization
80 of ultramafic rocks and carbonation of serpentinite are reasonably well understood,
81 but comprehension of the specific changes in fluid chemistry, which seem to be
82 controlled by thermodynamic as well as kinetic effects, remains haphazard.

83 We designed this study to examine concomitant changes in fluid chemistry
84 and secondary mineralogy from serpentinization to carbonation and to highlight the
85 role of two processes competing for dissolved carbon: magnesite precipitation and
86 methane formation. We analyzed the fluid chemistry of 11 sub-samples taken over
87 the course of the experiment and used thermodynamic relations to trace
88 mineralogical changes over time. After the experiment was terminated we
89 characterized the hydrothermal precipitates and compared the mineralogical and
90 fluid chemical results with thermodynamic predictions. It will be shown that the
91 injection of a CO₂-rich fluid into an active serpentinization system can cause a

92 cascade of mineral replacement reactions, which are accompanied by rapid changes
93 in fluid chemistry.

94

95 **2. EXPERIMENTAL SETUP AND ANALYTICAL METHODS**

96 We used a flexible-cell hydrothermal apparatus consisting of a gold bag
97 enclosed in a stainless steel pressure-containment vessel filled with water, which
98 acts as the pressure medium (Seyfried et al., 1987). One advantage of this apparatus
99 over a rigid steel reaction cell is that the gold bag itself is flexible allowing the
100 experiment to be conducted with no vapor headspace present. The reaction cell
101 connects to a thin titanium tube and a valve permitting periodic fluid sampling as
102 well as the injection of fluids during the experiment. The experiment itself can be
103 divided into two parts: initial serpentinization of olivine and, subsequently,
104 carbonation of the partly serpentinized olivine following the injection of the CO₂-
105 rich fluid. About 50 g of olivine (Fo₉₀) was rinsed with de-ionized water,
106 handpicked under a microscope, ground with a mortar and pestle, and thoroughly
107 wet-sieved to retain the fraction between 53 and 212 μm in size. The starting
108 solution was in equilibrium with the atmosphere and no attempt was made to
109 remove dissolved CO₂ or O₂ prior to the experiment. Initial serpentinization
110 involved 18.0 g olivine and 40.1 g of a 0.5 M NaCl solution, which was heated for 51
111 days at 300 °C and 35 MPa. A temperature of 300 °C was chosen because reaction
112 rates for serpentinization of olivine are fastest between ca. 270 °C and 300 °C
113 (Martin and Fyfe, 1970). However, reaction rates for mineral carbonation of olivine
114 are fastest at a temperature of ~185 °C (O'Connor et al., 2004). To take advantage of

115 increased carbonation rates the temperature was lowered to 230 °C and held at that
116 temperature for 7 days before a CO₂-rich fluid of seawater chlorinity was injected.
117 The injection fluid was prepared by pressurizing a steel tube of a known volume
118 filled with the NaCl solution with compressed CO_{2(g)} to 35 MPa. The fluid was then
119 injected into the reaction cell using a high-pressure pump. Carbonation went on for
120 33 days until most of the dissolved CO₂ was sequestered and the experiment was
121 terminated. Fluid samples (0.3 – 0.6 g each) were taken in 5 ml gas tight glass
122 syringes (Hamilton 1005 LT). Quantitative analyses of dissolved H₂, CO₂, and CH₄
123 were performed by extraction of the gases by adding ~1 ml pure He or N₂ to the
124 syringe and then injecting the headspace onto a gas chromatograph (cf. McCollom
125 and Seewald, 2003). Aliquots analyzed for CO₂ were acidified with phosphoric acid.
126 In addition to the acidified fluids, un-acidified aliquots of samples # CO-10-8 – CO-
127 10-11 were analyzed to approximate the $\Sigma\text{CO}_2/\text{CO}_{2(aq)}$. The concentrations of CO₂
128 were corrected to account for its partitioning between the headspace and fluid
129 phases within each individual syringe (Weiss, 1974). Fluid samples were analyzed
130 for dissolved components by inductively-coupled plasma mass spectrometry (ICP-
131 MS). The pH and dissolved SiO₂ were directly measured after a sample was taken.
132 The pH was measured using a micro combination electrode at 25 °C with an
133 uncertainty of approximately ±0.1 units of the reported value. Concentrations of
134 dissolved SiO₂ were determined spectrophotometrically using the heteropoly-blue
135 method with a Hach 2700 spectrophotometer at a wavelength of 815 nm.

136 After the experiment was terminated the mineral powder was filtered and
137 dried at room temperature before subsamples were taken for further analyses.

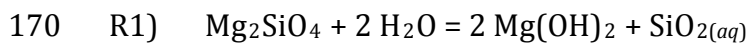
138 Mineralogical analysis of primary and secondary phases was carried out using a
139 confocal Raman microscope (Horiba Labram-HR), equipped with a 532nm laser and
140 a peltier-cooled CCD detector. A Zeiss Supra 40 field emission scanning electron
141 microscope (FE-SEM) and a Hitachi TM3000 SEM, along with a transmitted and
142 reflected light microscope were used for petrographic characterization of mineral
143 powders and polished mounts. Mineral compositions were analyzed using a
144 JEOL JXA-8530F Field-Emission Electron Probe Microanalyzer (FE-EPMA), operated
145 at 15kV acceleration voltage and 20nA beam current. The beam was fully focused
146 for olivine and 5 to 15 μm for all other phases to avoid beam damage. Raw data were
147 corrected using the CITZAF method (Armstrong, 1995). Equilibrium constants used
148 to construct activity diagrams (Figs. 1 & 4) were calculated with the computer code
149 SUPRCT92 (Johnson et al., 1992). The speciation calculations were carried out using
150 the software code EQ3/6 (Wolery, 1992) with a customized database assembled for
151 35 MPa appropriate for experimental conditions using SUPRCT92. Activity
152 coefficients of dissolved inorganic species were computed using the B-dot equation
153 with hard-core diameters, and B-dot and Debye-Hückel parameters from Wolery
154 and Jove-Colon (2004). Activity coefficients of neutral species are assumed to be
155 unity, except for non-polar gaseous species, for which the activity coefficients of CO_2
156 were adopted (Drummond, 1981). For a more detailed description of the databases
157 used in the present communication the interested reader is referred to McCollom
158 and Bach (2009) and Klein et al. (2009).

159

160 ***3. Results and Discussion***

161 3.1. Fluid Chemistry During Serpentinization

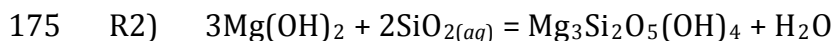
162 Fluid compositions of 11 sub-samples are summarized in Table 1. The
163 speciated activities of aqueous silica ($a\text{SiO}_{2(aq)}$), $a\text{Mg}^{2+}$ and $a\text{H}^+$ (i.e. the pH) can be
164 used to trace serpentinization reactions in hydrothermal experiments (e.g.,
165 Ogasawara et al., in press). The $\log a\text{Mg}^{++}/a\text{H}^{+^2} - \log a\text{SiO}_{2(aq)}$ diagram (Fig. 1)
166 shows a decrease of $\log a\text{SiO}_{2(aq)}$ from an initial value of -3.26 (sample # 1) 3 hours
167 after the experiment was initiated to -4.40 (sample # 2) after one week. The \log
168 $a\text{SiO}_{2(aq)}$ of samples 2, 3, and 5 closely matched the predicted equilibrium value for
169 the metastable reaction:



171 *olivine* *brucite*

172 while $\log a\text{Mg}^{++}/a\text{H}^{+^2}$ and $\log a\text{SiO}_{2(aq)}$ of sample # 4 is indicative of serpentine –
173 brucite equilibrium at 300 °C and 35 MPa:

174



176 *brucite* *serpentine*

177

178 The speciated fluid data of samples # 1 – 5 displayed in Fig. 1 indicate that $a\text{SiO}_{2(aq)}$,
179 Mg^{2+} , and pH are controlled by reactions 1 and 2 during serpentinization of olivine.
180 Concentrations of $\text{H}_2(aq)$ increased to 3.26 mM as the serpentinization proceeded,
181 suggesting that ferrous iron in olivine was oxidized to ferric iron in secondary
182 minerals. Indeed, Fe-bearing serpentine and minor amounts of magnetite were
183 detected among the solid reaction products (see section 3.3.). Trace amounts of

184 dissolved carbon ($\Sigma\text{CO}_2 < 1 \text{ mM}$) and $\text{CH}_{4(aq)}$ ($< 40\mu\text{M}$) were detected; however,
185 isotopic labeling experiments reveal that background levels of C are inevitable in
186 nominally C-free serpentinization experiments (McCollom and Seewald, 2001). The
187 pH (measured at room temperature) increased from ~ 8 to ~ 9 during
188 serpentinization, which is consistent with theoretical predictions (Klein et al., 2009)
189 and previously reported serpentinization experiments using olivine separates at
190 similar conditions (e.g., Anders, 2012). The corresponding in situ pH ranged
191 between 6.0 and 6.2. As expected, concentrations of dissolved Mg and Ca remained
192 low ($< 1 \text{ mM}$). Mg liberated by dissolution of olivine was consumed by the formation
193 of serpentine and brucite, whereas concentrations of dissolved Ca were low,
194 because olivine we used as the starting material contains only trace amounts (0.05
195 wt.%) of CaO (see Table 2). After 51 days we lowered the temperature to 230°C and
196 let the system react for 7 days before we injected the CO_2 -bearing fluid. The drop in
197 temperature caused minor readjustments in the fluid composition (Table 1). Sample
198 # 6, taken just before the injection, reveals a higher $a\text{Mg}^{++}/a\text{H}^{+^2}$ ratio than samples
199 taken at 300°C at a comparably low $a\text{SiO}_{2(aq)}$, which may suggest that the fluid was
200 re-equilibrating, but did not quite reach the brucite-serpentine equilibrium at 230
201 $^\circ\text{C}$ (see Fig. 1).

202

203 *3.2. Fluid Chemistry During Carbonation*

204 On day 58 21.8 g of fluid having 0.5 M of NaCl and 0.39 M $\text{CO}_{2(aq)}$ was injected
205 into the reaction cell. Just before the injection the reaction cell contained 18.8 g of
206 aqueous fluid with 0.8 mM $\text{CO}_{2(aq)}$. The resulting concentration of $\text{CO}_{2(aq)}$ in the

207 reaction cell following injection was approximately 209 mM. As shown in Figs. 1, 2,
208 and 4 (compare with. table 1), the injection of the CO₂-bearing fluid caused a
209 substantial and rapid change of the fluid chemistry. The pH (measured at 25 °C)
210 decreased from 9 just before the injection to about 6 after the injection. The
211 corresponding calculated in situ pH at 230 °C and 35 MPa was ~ 6 before the
212 injection and ~ 5.4 after the injection. Subsequently, the pH (at 25 °C) dropped
213 slightly below 6, but increased again to 6.8 before it decreased to 6.3 at the
214 termination of the experiment. Both acidified (with H₃PO₄) and non-acidified fluid
215 samples were analyzed for CO_{2(aq)} during this stage of the experiment. Consistent
216 with the slightly acidic pH measured at room temperature, the dominant carbon
217 species analyzed was CO_{2(aq)} (ca. 82 – 100 % of ΣCO₂). The activity of SiO_{2(aq)}
218 increased more than 2 orders of magnitude from log $a_{\text{SiO}_2(aq)} = -4.7$ (sample # 6)
219 prior to the injection to a maximum of -2.24 (sample # 8) after the injection, before
220 it eventually decreased again to about log $a_{\text{SiO}_2(aq)} = -3$. Since, the SiO_{2(aq)}
221 concentration of the injected fluid was at the detection limit of the method (0.01
222 ppm), dilution during injection would have caused a decrease in $a_{\text{SiO}_2(aq)}$. However,
223 the increase in $a_{\text{SiO}_2(aq)}$ following injection indicates dissolution of Mg-silicates and
224 liberation of silica. The $a_{\text{H}_2(aq)}$ decreased from log $a_{\text{H}_2(aq)} = -2.49$ before the
225 injection to -3.07 at the termination of the experiment. This decrease is consistent
226 with a dilution of the reacting fluid during injection. Remarkably, however,
227 continued generation of H_{2(aq)} was not observed after the injection, which suggests
228 that serpentinization and accompanying oxidation of Fe ceased.

229 Previous serpentinization experiments using ^{13}C -labeled fluid reactants have
230 shown that background sources liberate methane at micro-molar levels (McCollom
231 and Seewald, 2001). These experiments revealed that only a small fraction of the
232 methane generated was present as $^{13}\text{CH}_{4(aq)}$, which means the main source of $\text{CH}_{4(aq)}$
233 is reduced carbon already present in the starting materials (cf. Jones et al., 2010).
234 We did not use ^{13}C -labeled reactants in the present study, since trace amounts of
235 carbon present before the injection would not significantly affect mineral
236 carbonation or methane formation. As expected, the concentrations of $\text{CH}_{4(aq)}$
237 measured during serpentinization ranged at micro-molar levels (Jones et al., 2010;
238 McCollom and Seewald, 2001). Measured concentrations of $\text{CH}_{4(aq)}$ decreased from
239 $\sim 37 \mu\text{M}$ before the injection to $\sim 18 \mu\text{M}$ immediately after the injection, which can
240 be explained by dilution with the methane-free injection fluid. Although the
241 calculated affinity A of methane formation at the expense of $\text{CO}_{2(aq)}$ and $\text{H}_{2(aq)}$ is
242 large (e.g., sample # 8 $A = 4108 \text{ J/mol}$, assuming activity coefficients of $\text{H}_{2(aq)}$ and
243 $\text{CH}_{4(aq)} = 1.14$) after the injection, concentrations remained low and virtually
244 constant at $\sim 20 \mu\text{mol/kg}$ until the experiment was terminated. Because the
245 reduction of CO_2 to $\text{CH}_{4(aq)}$ appears to be sluggish under the experimental
246 conditions, we decoupled the redox reactions involving the reduction of $\text{CO}_{2(aq)}$ to
247 hydrocarbons in the speciation calculations. Concentrations of dissolved Mg were
248 low during serpentinization ($< 1 \text{ mmol/kg}$), increased noticeably during initial
249 carbonation to about 3 mmol/kg , and then decreased to $< 2 \text{ mmol/kg}$ towards the
250 end of the experiment. Slightly lower concentrations of Mg have been measured in a
251 flow-through carbonation experiment using sintered, but un-serpentinized dunite

252 as the feedstock at 160 °C and 12 MPa (Andreani et al., 2009). Concentrations of
253 dissolved Ca were slightly higher during serpentinization (< 0.65 mmol/kg) than
254 during carbonation (< 0.27 mmol/kg), reflecting the incorporation of Ca in
255 precipitating carbonate.

256

257 *3.3. Solid Reaction Products*

258 Minerals identified using FE-EMPA and Raman spectroscopy include
259 magnesite, serpentine, magnetite, minor talc, and relict olivine (Fig. 3).
260 Representative compositions of these minerals are presented in Table 2. No other
261 minerals were detected using XRD analysis. Although speciation calculations of fluid
262 sample # 8 suggest quartz saturation (Figs. 1 & 4) for a short period of time, no
263 quartz was observed in the final reaction products. The dominant serpentine
264 polymorph found is chrysotile (Fig. 3). In addition, minor lizardite was detected
265 using Raman analysis. Individual chrysotile fibers appear to have remained
266 unaltered during carbonation, have a diameter of ca. 10 - 100 nm, and are several
267 μm in length (Fig. 3). Although chrysotile apparently formed chiefly during the
268 initial serpentinization stage of the experiment, it is conceivable that some
269 additional chrysotile may have grown during carbonation via silication of brucite
270 (R2). The anhydrous sum of oxides of the chrysotile analysis approximates 80 wt.%,
271 whereas the ideal for chrysotile and lizardite is about 87-88 wt.%, depending on Fe
272 and Al contents. Evans et al. (2012) point out that low anhydrous totals of
273 serpentine are not uncommon. The low totals of the chrysotile analyses (table 2) are
274 most likely related to a combination of imperfect sample preparation, the minute

275 crystal size, porosity, and the CITZAF correction procedure. To facilitate comparison
276 of our serpentine analysis with those from the literature we recalculated the
277 chemical composition of serpentine to 87 wt.% (table 2). Serpentine is Fe-bearing
278 (table 2) having an X_{Mg} of ca. 0.93. Minor talc is finely intergrown with serpentine on
279 a submicron scale (Fig. 3), making it difficult to obtain accurate chemical analysis.
280 With the exception of one analysis, most electron microprobe measurements were
281 mixtures of serpentine and talc, having (Mg+Fe)/SiO₂ molar ratios ranging between
282 1.4 and 1.04. Talc is Fe-bearing and exhibits an X_{Mg} of 0.92 (table 2). The lack of
283 H_{2(aq)} generation during carbonation suggests that the iron incorporated into talc
284 during the second half of the experiment is chiefly ferrous. Magnetite forms
285 euhedral octahedra up to a few tens of microns in size (Fig. 3). Although the absence
286 of increasing H_{2(aq)} levels during the carbonation stage suggest that the magnetite
287 precipitated exclusively during serpentinization, the crystals do not show any signs
288 of resorption or signs of replacement by hematite, as it is found in many carbonate-
289 altered serpentinites (Frost, 1985). Magnesite forms colorless to white sub- to
290 euhedral crystals that measure < 1µm to several hundred micrometers in diameter
291 (Fig. 3). Magnesite is Fe-bearing and has an X_{Mg} of ~ 0.92 (table 2). Some crystals,
292 however, reveal a distinct zoning in X_{Mg} within a range of 0.91 – 0.94. Due to the low
293 CaO contents of the overall system, the concentrations of CaO in magnesite are
294 below 0.1 wt.%.

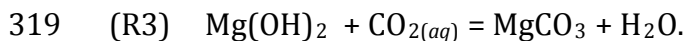
295

296

297 *3.4. Reaction Pathway and Magnesite Precipitation Over Time*

298 The changes in fluid chemistry over time can be linked with the observed
299 secondary mineralogy using speciation calculations and thermodynamic phase
300 equilibria. Figure 4 displays the MgO-SiO₂-H₂O-CO₂ (MSHC) phase equilibria at
301 230 °C and 35 MPa in a log $a\text{CO}_{2(aq)}$ – log $a\text{SiO}_{2(aq)}$ plane (cf. Greenwood, 1967; Klein
302 and Garrido, 2011). Also plotted are the speciated $a\text{SiO}_{2(aq)}$ and $a\text{CO}_{2(aq)}$ of fluids
303 sampled during the experiment. The activities of CO_{2(aq)} and SiO_{2(aq)} of fluid sample
304 # 06 (representing the serpentinization = pre-carbonation stage) plot within the
305 stability field of chrysotile in vicinity of the serpentine–brucite–magnesite quasi-
306 invariant (assuming that $a\text{H}_2\text{O} \approx 1$) point and the metastable olivine–magnesite
307 univariant phase boundary (the term phase boundary is used synonymously with
308 line of equal activities). Previous serpentinization experiments conducted at similar
309 conditions yielded mainly serpentine, brucite, minor magnetite, and traces of
310 carbonate in addition to relict olivine (e.g., McCollom and Seewald, 2001). The
311 $a\text{CO}_{2(aq)}$ and $a\text{SiO}_{2(aq)}$ of sample # 6 in Figure 4 are consistent with this dis-
312 equilibrium assemblage, which we assume represents the solid starting material
313 prior to the injection of the CO₂-rich fluid. Already two hours after the injection,
314 $a\text{CO}_{2(aq)}$ and $a\text{SiO}_{2(aq)}$ of sample # 07 fall in close vicinity of the metastable branch of
315 the phase boundary of serpentine and talc within the stability field of magnesite
316 (Figs. 1 & 4). Brucite is unstable at such high $a\text{CO}_{2(aq)}$ and $a\text{SiO}_{2(aq)}$, and will undergo
317 carbonation to magnesite:

318

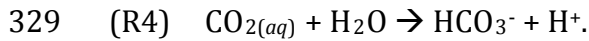


320

321 Hydrothermal experiments conducted by Hövelmann et al. (2012) and Zhao et al.
322 (1997) have demonstrated that the dissolution of brucite and simultaneous
323 precipitation of Mg-carbonate can proceed on the scale of minutes to hours. Thus, it
324 seems likely that brucite underwent complete carbonation to magnesite shortly
325 after the injection.

326 The rapid drop in pH after the injection of the CO₂-rich fluid was most likely due to
327 the reaction

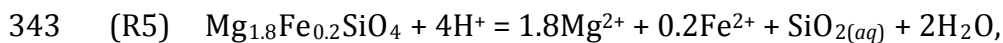
328



330

331 A lower pH, in turn, can cause enhanced dissolution of Mg-silicates. However,
332 chrysotile fibers remained virtually unaltered in the present experiment, whereas
333 olivine shows abundant dissolution pits (Fig. 3). This finding is consistent with the
334 notion that carbonation rates of serpentine (including dissolution of serpentine and
335 precipitation of magnesite) are more than 10 times slower than carbonation rates of
336 olivine at elevated temperatures and pressures (Kelemen & Matter, 2008, Kelemen
337 et al., 2011; Gerdemann et al., 2007; O'Connor et al., 2004; Hövelmann et al., 2012)
338 (Daval et al., 2013). Likewise, it is conceivable that carbonation rates of talc are
339 similar to those of serpentine on laboratory timescales. On the basis of our
340 petrographic results and previous experiments it seems likely that a lowered pH
341 (due to R4) can cause enhanced olivine dissolution,,

342



344 olivine

345

346 which then liberates Mg^{2+} , Fe^{2+} , and $SiO_{2(aq)}$ to the solution. Dissolved Mg^{2+} and Fe^{2+}
347 will react with $CO_{2(aq)}$ to form Fe-bearing magnesite. Efficient olivine dissolution
348 and relatively sluggish talc precipitation (cf. Hänchen et al., 2006; Saccocia et al.,
349 2009) lead to the concomitant sharp increase in $aSiO_{2(aq)}$, which culminated in
350 quartz saturation (sample # 8, Figs. 1 & 4). However, quartz was not found among
351 the solid reaction products. The lack of quartz can be explained by low levels of
352 super-saturation, sluggish precipitation kinetics, and/or by its dissolution before the
353 experiment was terminated. The decrease in $aSiO_{2(aq)}$ and $aCO_{2(aq)}$ of all subsequent
354 samples suggests that talc precipitated together with magnesite, which was
355 confirmed by spectroscopic evidence. Note that sample # 10 has a higher log
356 aMg^{++}/aH^{+^2} than samples # 9 and 11. This behavior is possibly an artifact. Since the
357 measured Mg concentration of sample 10 appears to be reasonable, falling between
358 samples 9 and 11, it seems the pH is too high. An increased pH could be explained,
359 e.g., by removal of headspace CO_2 , driving reaction 4 to the left..

360 The magnesite precipitation rate can be approximated with the decrease of
361 $aCO_{2(aq)}$ over time, because chemical analysis of the fluid revealed no hydrocarbon
362 formation after the injection, so that carbonate precipitation was the only significant
363 sink for $CO_{2(aq)}$ in the experiment. It was found that the consumption of $CO_{2(aq)}$ and
364 precipitation of magnesite can be well described with a simple nucleation and
365 growth law of the form $X = 1 - e^{(Kt^n)}$, where X is the fraction of $CO_{2(aq)}$ consumed
366 or fraction of magnesite precipitated, K contains terms related to the shape of the

367 product, the number of growth dimensions, and nucleation rate, t represents time,
368 and the exponent n is a function of the number and type of time dependent
369 processes participating in the reaction (Avrami, 1939; Avrami, 1940). When $-\ln (ln$
370 $(1-x))$ is plotted against $ln t$, the rate constant K can be determined from the
371 intercept of the line on the ordinate (Fig. 5). Linearization of the Avrami equation
372 yields a rate constant $K = 2.5 \times 10^{-6} \text{ sec}^{-1}$ and a growth order of $n = 0.78$ (Fig. 5).
373 Avrami-type precipitation reactions are interpreted to proceed in 3 distinct stages
374 1) a slow initial nucleation stage, which is followed by 2) an accelerating growth
375 stage until 3) one of the reactants is exhausted or the reaction approaches
376 equilibrium and precipitation slows down. All 3 stages are apparent in the data as
377 shown in Figure 6 (green line); however, stage 1 lasted only a few minutes before
378 magnesite precipitation accelerated in stage two. In other words magnesite began to
379 precipitate almost instantaneously after the injection of the CO_2 -rich fluid while
380 serpentinization ceased. Stage 2 is the main carbonation phase and lasted about 6
381 days in the present experiment before most of the $\text{CO}_{2(aq)}$ was consumed and
382 magnesite precipitation slowed down. Shown for comparison is a fit calculated by
383 Kelemen et al (2011) to the data of O'Connor et al. (2004) on the extent of olivine
384 carbonation as a function of time (blue line in Fig. 6). Experiments of O'Connor et al
385 (2004) were conducted at 185°C and $15 \text{ MPa } P_{\text{CO}_2}$, in aqueous solutions with 1M
386 NaCl and $0.64\text{M } \text{NaHCO}_3$. Consistent with previous assessments of olivine
387 carbonation (Kelemen et al., 2011; Kelemen and Matter, 2008), reaction rates slow
388 down at temperatures higher than 185°C ; however, a direct comparison of both
389 datasets remains difficult due to differences in the experimental setups (in our

390 experiment $a\text{CO}_{2(aq)}$ decreases over time while $a\text{CO}_{2(aq)}$ in O'Connor et al.'s
391 experiment remains constant).

392

393

394 **4. SUMMARY AND CONCLUSIONS**

395 The present study was designed to trace the changes in fluid chemistry and
396 concomitant changes in mineralogy from serpentinization to carbonation as a
397 function of time. Serpentinization of olivine resulted in the formation of serpentine
398 (mainly chrysotile), brucite, and magnetite (\pm magnesite), along with significant, but
399 relatively low concentrations of $\text{H}_{2(aq)}$. The injection of a CO_2 -rich fluid caused a
400 rapid change in fluid chemistry and a cessation of serpentinization, as suggested by
401 the virtually stagnant levels of $a\text{H}_{2(aq)}$ and $\text{CH}_{4(aq)}$ during carbonation. The injected
402 fluid was in sharp disequilibrium with brucite, which resulted in its replacement by
403 Fe-bearing magnesite (cf. Hövelmann et al., 2012; Zhao et al, 1997). Dissociation of
404 carbonic acid caused a decrease in pH, which led in turn to an enhanced dissolution
405 of olivine, while serpentine remained apparently unaltered. Dissolution of olivine
406 liberated Mg^{2+} , Fe^{2+} , and $\text{SiO}_{2(aq)}$ to the CO_2 -rich fluid, which promoted Fe-bearing
407 magnesite and talc precipitation. However, the small amount of talc present among
408 the reaction products suggests that its precipitation proceeded rather sluggishly. In
409 combination, efficient olivine dissolution and sluggish talc precipitation caused a
410 rapid increase in $a\text{SiO}_{2(aq)}$ to temporary quartz saturation.

411 Carbon dioxide is present in hydrothermal fluids at sub-seafloor pressures
412 and temperatures, and numerous laboratory studies have confirmed that $\text{CO}_{2(aq)}$ can

413 be reduced to methane and other hydrocarbons under reducing conditions (Horita
414 and Berndt, 1999; McCollom and Seewald, 2001; McCollom and Seewald, 2003;
415 McCollom and Seewald, 2006; Seewald et al., 2006). These experiments reveal that
416 the conversion of $\text{CO}_{2(aq)}$ to $\text{CH}_{4(aq)}$, unless catalyzed by Ni-Fe alloys, is rather
417 sluggish and proceeds through a series of incremental reactions, with formic acid,
418 carbon monoxide, formaldehyde, and methanol forming as intermediate carbon
419 compounds (Seewald et al., 2006). Ni-Fe alloys, sulfur-poor sulfides, Cr-spinel, and
420 Fe-oxides, all of which are considered potential surface catalysts for Sabatier or
421 Fischer-Tropsch type reactions are indeed present in serpentinite (Alt and Shanks,
422 1998; Beard and Hopkinson, 2000; Dick and Gillete, 1976; Frost, 1985; Klein and
423 Bach, 2009; Ramdohr, 1950), but usually do not exceed 0.1 vol. %. However, their
424 minute, sub-micron grain size and virtually ubiquitous dispersion in abyssal
425 serpentinite (Klein and Bach, 2009) can provide substantial surface area for
426 potential catalysis. Although McCollom and Seewald (2001) reported the
427 precipitation of carbonate during their study on the reduction of CO_2 during
428 serpentinization, experimental studies designed to examine mineral carbonation of
429 olivine, serpentine, or other Mg-silicates under hydrothermal conditions have not
430 reported on the formation of methane or other hydrocarbons during the
431 experiments (Alexander et al., 2007; Andreani et al., 2009; Bearat et al., 2006;
432 Bearat et al., 2002; Dufaud et al., 2009; Gerdemann et al., 2007; Hövelmann et al.,
433 2011; Hövelmann et al., 2012; O'Connor et al., 2004; Park and Fan, 2004; Wolf et al.,
434 2003; Zhao et al., 2010). As a consequence, there are few experimental constraints
435 on the relationships between carbonate mineral formation and competing carbon

436 reduction reactions in serpentinizing systems. The present experiment highlights
437 that magnesite precipitation is markedly faster than the reduction of CO₂ to CH₄
438 (even in the presence of potential surface catalysts such as magnetite), if a CO₂-rich
439 fluid is introduced into mildly reducing serpentinization systems. Methane
440 formation might be more significant in more reducing serpentinization systems in
441 the presence of more effective surface catalysts such as Ni-Fe alloy (cf. Horita and
442 Berndt, 1999); however, it seems unlikely that this process dominates over
443 magnesite precipitation even at more reducing conditions.

444 Because CH₄ has a much higher global warming potential than CO₂ (e.g., 72
445 times higher over a period of 20 years, Forster et al., 2007), an uncontrolled release
446 of large quantities of CH₄ during engineered *in situ* mineral carbonation of
447 ultramafic rocks is unwanted. In this respect the results of our experiment
448 tentatively suggest that CH₄ formation will likely be limited by the more efficient
449 precipitation of magnesite at conditions similar to those of our experiment.
450 However, silicification reactions due to increased *a*SiO_{2(aq)} (c.f. Klein and Garrido,
451 2011) as well as acidification of interacting fluids must be taken into account, when
452 *in situ* carbonation of peridotite is considered.

453

454 **Acknowledgments**

455 We would like to thank M. Sulanowska for sample preparation and XRD analysis. Jim
456 Eckert is thanked for his support with electron microprobe analysis. The editorial
457 handling by Tim Elliott is much appreciated. We thank Dionysis Foustoukos and an
458 anonymous reviewer for helpful suggestions. This work was supported by an Ocean

459 Ridge Initiative Research Award at WHOI (to FK) and NSF Marine Geology and
460 Geophysics award OCE-0927744 (TMM).

461

462

463

464

465 **FIGURE CAPTIONS**

466 **Figure 1)** Activity-activity diagram for fluid-mineral equilibria in the MgO-SiO₂-H₂O
467 system calculated using the software package SUPCRT92 (Johnson et al., 1902) for a
468 pressure of 35 MPa. Gray lines denote equilibria at 300 °C, black lines denote
469 equilibria at 230 °C. Mineral names are abbreviated as follows: Brc = brucite, Ctl =
470 chrysotile, Fo =forsterite, Qtz = quartz, Tlc = talc. The quartz-SiO_{2(aq)} equilibrium is
471 illustrated only for 230 °C. Also shown are the speciated compositions of fluid
472 samples # 1 – 11 computed with the software code EQ3/6 (Wolery, 1992). Gray
473 diamonds denote fluids speciated for a temperature of 300°C (samples 1-5), orange
474 squares denote samples speciated for a temperature of 230 °C (samples 6-11).
475 Dashed lines illustrate metastable reactions at the experimental conditions. Note the
476 marked change in $a\text{SiO}_{2(aq)}$ and $a\text{Mg}^{2+}/a\text{H}^{+2}$ before (samples 1-6) and after
477 (samples 8-11) the injection of a CO₂-rich fluid. See text for discussion.

478

479 **Figure 2)** Measured (unspeciated) fluid composition as a function of time. Changes
480 in fluid composition were observed when the temperature was lowered from 300 to
481 230 °C as well as after the injection of the CO₂-rich fluid.

482

483 **Figure 3)** Back-scattered electron images of feedstock olivine and solid reaction
484 products. a) Sheets of chrysotile (Ctl) fibers (gray) and magnetite (Mag) octahedra
485 (white), powder sample. b) Olivine (Ol) exhibits dissolution features and Ctl
486 overgrowth, powder sample. c) Euhedral magnesite (Mgs) covering Ctl / talc (Tlc)
487 intergrowths, powder sample. d) Ol, Mgs, and Ctl in cross-section, polished grain

488 mount. e) Cross-section of Ctl-fiber aggregate, polished grain mount. f) Intergrowths
489 of Tlc and Ctl, white crystal is Mag, polished grain mount.

490

491 **Figure 4)** Log activity-activity diagram depicting the stability fields and lines of
492 equal activity of phases in the system $\text{MgO-SiO}_2\text{-H}_2\text{O-CO}_2$ calculated for 230 °C and
493 35 MPa using the software code SUPCRT92 (Johnson et al., 1992). The black dashed
494 line shows the metastable branch of the serpentine-talc equilibrium (reaction R6).
495 The blue dashed line denotes the metastable olivine–magnesite equilibrium. The
496 solubility of quartz (red line) was calculated using the thermodynamic data of
497 Rimstidt (1997). Also shown are the speciated $\text{SiO}_{2(aq)}$ and $\text{aCO}_{2(aq)}$ activities of fluid
498 samples. Sample # 6 represents the serpentinization (pre-injection) stage, samples
499 # 7-11 represent the carbonation (i.e. post-injection) stage. $\text{SiO}_{2(aq)}$ and $\text{CO}_{2(aq)}$
500 activities change markedly and follow roughly the (metastable) lines of equal
501 activity of brucite, chrysotile, talc, magnesite, olivine, and quartz.

502

503 **Figure 5)** A plot of $\ln(\ln-1-x)$ against $\ln t$ (time in seconds), where x is the fraction of
504 CO_2 consumed (equal to the amount of magnesite precipitated). If reaction rates
505 conform the Avrami rate law $\ln(\ln-1-x)$ against $\ln t$ is linear (Putnis, 1992). The
506 slope equals the constant n , and the intercept at the ordinate gives the rate constant
507 k .

508

509 **Figure 6)** Data (yellow circles) and best fit (green line) for the fraction X of $\text{CO}_{2(aq)}$
510 consumed (\approx fraction of magnesite precipitated) as a function of time. The rate

511 constant $K = 2.5 \times 10^{-6} \text{ s}^{-1}$ and the growth order $n = 0.78$. Magnesite precipitation can
512 be represented by 3 distinct stages, a relatively slow initial nucleation stage (stage
513 I), which is followed by an accelerating growth stage (stage II) until most of the
514 $\text{CO}_{2(aq)}$ is consumed and the precipitation slows down (stage III). Shown for
515 comparison is a fit calculated by Kelemen et al (2011) to the data of O'Connor et al.
516 (2004) on the extent of olivine carbonation as a function of time (gray curve).
517 Experiments of O'Connor et al (2004) were conducted at 185°C and 150 bars P_{CO_2} ,
518 in aqueous solutions with 1M NaCl and 0.64M NaHCO_3 .

519

520

521 **References**

- 522 Abrajano, T.A. et al., 1988. Methane-hydrogen gas seeps, Zambales Ophiolite,
523 Philippines: Deep or shallow origin? *Chemical Geology*, 71(1-3): 211-222.
- 524 Alexander, G., Mercedes Maroto-Valer, M., Gafarova-Aksoy, P., 2007. Evaluation of
525 reaction variables in the dissolution of serpentine for mineral carbonation.
526 *Fuel*, 86(1,Ä2): 273-281.
- 527 Alt, J.C., Shanks, W.C., 1998. Sulfur in serpentinized oceanic peridotites:
528 Serpentinization processes and microbial sulfate reduction. *Journal of*
529 *Geophysical Research*, 103: 9917-9929.
- 530 Anders, H., 2012. Experimental investigations of interactions between saltwater and
531 ultramafic rocks in hydrothermal systems, University of Bremen, Bremen.
- 532 Andreani, M. et al., 2009. Experimental study of carbon sequestration reactions
533 controlled by the percolation of CO_2 -rich brine through peridotites.
534 *Environmental Science & Technology*, 43(4): 1226-1231.
- 535 Armstrong, J.T., 1995. CITZAF: A package of correction programs for the quantitative
536 electron microbeam X-ray analysis of thick polished materials, thin films, and
537 particles. *Microbeam Analysis*, 4: 177-200.
- 538 Avrami, M., 1939. Kinetics of Phase Change. I General Theory. *J. Chem. Phys.*, 7(12):
539 1103.
- 540 Avrami, M., 1940. Kinetics of phase change. II transformation-time relations for
541 random distribution of nuclei. *J. Chem. Phys.*, 8(2): 212.
- 542 Bearat, H. et al., 2006. Carbon sequestration via aqueous olivine mineral
543 carbonation: role of passivating layer formation. *Environmental Science &*
544 *Technology*, 40(15): 4802-4808.

545 Bearat, H., McKelvy, M.J., Chizmeshya, A.V.G., Sharma, R., Carpenter, R.W., 2002.
546 Magnesium Hydroxide Dehydroxylation/Carbonation Reaction Processes:
547 Implications for Carbon Dioxide Mineral Sequestration. *Journal of the*
548 *American Ceramic Society*, 85(4): 742-748.

549 Beard, J.S., Hopkinson, L., 2000. A fossil, serpentinization-related hydrothermal vent,
550 Ocean Drilling Program Leg 173, Site 1068 (Iberia Abyssal Plain): Some
551 aspects of mineral and fluid chemistry. *J. Geophys. Res.*, 105(B7): 16527-
552 16539.

553 Boschi, C., Dini, A., Dallai, L., Ruggieri, G., Gianelli, G., 2009. Enhanced CO₂-mineral
554 sequestration by cyclic hydraulic fracturing and Si-rich fluid infiltration into
555 serpentinites at Malenrata (Tuscany, Italy). *Chemical Geology*, 265(1-2):
556 209-226.

557 Cannat, M., Fontaine, F., Escartin, J., 2010. Serpentinization and associated hydrogen
558 and methane fluxes at slow spreading ridges. In: Rona, P.A., Devey, C.W.,
559 Dymont, J., Murton, B.J. (Eds.), *Diversity of hydrothermal systems on slow*
560 *spreading ocean ridges. Geophysical Monograph Series 188*, pp. 241-264.

561 Charlou, J.-L., Donval, J.-P., Fouquet, Y., Jean-Baptiste, P., Holm, N., 2002.
562 Geochemistry of high H₂ and CH₄ vent fluids issuing from ultramafic rocks at
563 the Rainbow hydrothermal field (36°14'N, MAR). *Chemical Geology*, 191:
564 345-359.

565 Chidester, A.H., Cady, W.M., 1972. Origin and emplacement of Alpine-type ultramafic
566 rocks. *Nature*, 240: 27-31.

567 Cipolli, F., Gambardella, B., Marini, L., Ottonello, G., Vetuschi Zuccolini, M., 2004.
568 Geochemistry of high-pH waters from serpentinites of the Gruppo di Voltri
569 (Genova, Italy) and reaction path modeling of CO₂ sequestration in
570 serpentinite aquifers. *Applied Geochemistry*, 19(5): 787-802.

571 Coleman, R.G., 1977. *Ophiolites: ancient oceanic lithosphere?* Springer Verlag,
572 Berlin, 229 pp.

573 Daval, D., Hellmann, R., Martinez, I., Gangloff, S., Guyot, F.o., 2013. Lizardite
574 serpentine dissolution kinetics as a function of pH and temperature,
575 including effects of elevated pCO₂. *Chemical Geology*, 351(0): 245-256.

576 Dick, H.J.B., Gillette, H., 1976. Josephinite: specimens from the earth's core? -- a
577 discussion. *Earth and Planetary Science Letters*, 31(2): 308-311.

578 Dick, H.J.B., Lin, J., Schouten, H., 2003. An ultraslow-spreading class of ocean ridge.
579 *Nature*, 426: 405-412.

580 Drummond, S.E., Jr., 1981. *Boiling and Mixing of Hydrothermal Fluids: Chemical*
581 *Effects on Mineral Precipitation*, The Pennsylvania State University,
582 University Park.

583 Dufaud, F., Martinez, I., Shilobreeva, S., 2009. Experimental study of Mg-rich silicates
584 carbonation at 400 and 500°C and 1 kbar. *Chemical Geology*, 265(1-2): 79-
585 87.

586 Evans, B.W., Dyar, M.D., Kuehner, S.M., 2012. Implications of ferrous and ferric iron
587 in antigorite. *American Mineralogist*, 97(1): 184-196.

588 Forster, P. et al., 2007. Changes in atmospheric constituents and in radiative forcing.
589 *Climate change*, 20.

590 Foustoukos, D.I., Seyfried, W.E., 2004. Hydrocarbons in hydrothermal vent fluids:
591 the role of chromium-bearing catalysts. *Science*, 304: 1002-1005.

592 Frost, B.R., 1985. On the stability of sulfides, oxides and native metals in
593 serpentinite. *Journal of Petrology*, 26: 31-63.

594 Fryer, P., Gharib, J., Ross, K., Savov, I., Mottl, M.J., 2006. Variability in serpentinite
595 mudflow mechanisms and sources: ODP drilling results on Mariana forearc
596 seamounts. *Geochem. Geophys. Geosyst.*, 7(8): Q08014.

597 Gerdemann, S.J., O'Connor, W.K., Dahlin, D.C., Penner, L.R., Rush, H., 2007. Ex Situ
598 Aqueous Mineral Carbonation. *Environmental Science & Technology*, 41(7):
599 2587-2593.

600 Giammar, D.E., Bruant, J.R.G., Peters, C.A., 2005. Forsterite dissolution and magnesite
601 precipitation at conditions relevant for deep saline aquifer storage and
602 sequestration of carbon dioxide. *Chemical Geology*, 217(3-4): 257-276.

603 Greenwood, H.J., 1967. Mineral equilibria in the system MgO-SiO₂-H₂O-CO₂. In:
604 Abelson, P.H. (Ed.), *Researches in Geochemistry*. John Wiley and Sons, New
605 York, pp. 543-567.

606 Griffis, R., 1972. Genesis of a magnesite deposit, Deloro Twp., Ontario. *Econ. Geol.*,
607 67: 63-71.

608 Hänchen, M., Prigiobbe, V., Storti, G., Seward, T.M., Mazzotti, M., 2006. Dissolution
609 kinetics of fosteritic olivine at 90-150 °C including effects of the presence of
610 CO₂. *Geochimica et Cosmochimica Acta*, 70(17): 4403-4416.

611 Hansen, L.D., Dipple, G.M., Gordon, T.M., Kellett, D.A., 2005. Carbonated serpentinite
612 (listwanite) at Atlin, British Columbia: a geological analogue to carbon
613 dioxide sequestration. *The Canadian Mineralogist*, 43: 225-239.

614 Hess, H.H., 1933. The problem of serpentinitization and the origin of certain
615 chrysotile asbestos, talc, and soapstone deposits. *Economic Geology*, 28(7):
616 634-657.

617 Horita, J., Berndt, M.E., 1999. Abiogenic methane formation and isotopic
618 fractionation under hydrothermal conditions. *Science*, 285: 1055-1057.

619 Hövelmann, J., Austrheim, H., Beinlich, A., Anne Munz, I., 2011. Experimental study of
620 the carbonation of partially serpentinitized and weathered peridotites.
621 *Geochimica et Cosmochimica Acta*, 75(22): 6760-6779.

622 Hövelmann, J., Putnis, C.V., Ruiz-Agudo, E., Austrheim, H., 2012. Direct Nanoscale
623 Observations of CO₂ Sequestration during Brucite [Mg(OH)₂] Dissolution.
624 *Environmental Science & Technology*, 46(9): 5253-5260.

625 IPCC, 2005. IPCC special report on carbon dioxide capture and storage. Cambridge
626 University Press, Cambridge, New York.

627 Irwin, W.P., Barnes, I., 1980. Tectonic relations of carbon dioxide discharges and
628 earthquakes. *J. Geophys. Res.*, 85(B6): 3115-3121.

629 Johnson, J.W., Oelkers, E.H., Helgeson, H.C., 1992. SUPCRT92: A software package for
630 calculating the standard molal thermodynamic properties of minerals, gases,
631 aqueous species, and reactions from 1-5000 bars and 0-1000°C. *Computers &
632 Geosciences*, 18: 899-947.

633 Jones, L.C., Rosenbauer, R., Goldsmith, J.I., Oze, C., 2010. Carbonate control of H₂ and
634 CH₄ production in serpentinitization systems at elevated P-Ts. *Geophysical
635 Research Letters*, 37(14): L14306.

636 Kelemen, P.B. et al., 2011. Rates and mechanisms of mineral carbonation in
637 peridotite: natural processes and recipes for enhanced, in situ CO₂ capture
638 and storage. *Annual Review of Earth and Planetary Sciences*, 39(1): 545-576.
639 Kelemen, P.B., Matter, J.M., 2008. In situ carbonation of peridotite for CO₂ storage.
640 *PNAS*, 105: 17295-17300.
641 Klein, F., Bach, W., 2009. Fe-Ni-Co-O-S phase relations in peridotite seawater
642 interactions. *Journal of Petrology*, 50(1): 37-59.
643 Klein, F. et al., 2009. Iron partitioning and hydrogen generation during
644 serpentinization of abyssal peridotites from 15°N on the Mid-Atlantic Ridge.
645 *Geochimica et Cosmochimica Acta*, 73(22): 6868-6893.
646 Klein, F., Garrido, C.J., 2011. Thermodynamic constraints on mineral carbonation of
647 serpentinized peridotite. *Lithos*, 126(3-4): 147-160.
648 Koons, P.O., 1981. A study of natural and experimental metasomatic assemblages in
649 an ultramafic-quartzofeldspathic metasomatic system from the Haast Schist,
650 South Island, New Zealand. *Contributions to Mineralogy and Petrology*, 78:
651 189-195.
652 Korzhinskii, D.S., 1959. Physicochemical basis of the analysis of the paragenesis of
653 minerals. Consultants Bureau, N.Y.
654 Martin, B., Fyfe, W.S., 1970. Some experimental and theoretical observations on the
655 kinetics of hydration reactions with particular reference to serpentinization.
656 *Chemical Geology*, 6: 185-202.
657 McCollom, T.M., Bach, W., 2009. Thermodynamic constraints on hydrogen
658 generation during serpentinization of ultramafic rocks. *Geochimica et*
659 *Cosmochimica Acta*, 73(3): 856-875.
660 McCollom, T.M., Seewald, J.S., 2001. A reassessment of the potential for reduction of
661 dissolved CO₂ to hydrocarbons during serpentinization of olivine. *Geochim.*
662 *Cosmochim. Acta*, 65: 3769-3778.
663 McCollom, T.M., Seewald, J.S., 2003. Experimental constraints on the hydrothermal
664 reactivity of organic acids and acid anions: I. formic acid and formate.
665 *Geochimica Cosmochimica Acta*, 67: 3625-3644.
666 McCollom, T.M., Seewald, J.S., 2006. Carbon isotope composition of organic
667 compounds produced by abiotic synthesis under hydrothermal conditions.
668 *Earth and Planetary Science Letters*, 243: 74-84.
669 O'Connor, W.K., Dahlin, D.C., Rush, G.E., Gerdemann, S.J., Nilsen, D.N., 2004. Final
670 report: Aqueous mineral carbonation. DOE/ARC-TR-04-002: Albany, OR,
671 Office of Process Development, Albany Research Center, Office of Fossil
672 Energy, US DOE, p. 21 pages plus appendices.
673 Ogasawara, Y., Okamoto, A., Hirano, N., Tsuchiya, N., in press. Coupled reactions and
674 silica diffusion during serpentinization. *Geochimica et Cosmochimica Acta*(0).
675 Park, A.-H.A., Fan, L.-S., 2004. CO₂ mineral sequestration: physically activated
676 dissolution of serpentine and pH swing process. *Chemical Engineering*
677 *Science*, 59(22-23): 5241-5247.
678 Proskurowski, G. et al., 2008. Abiogenic Hydrocarbon Production at Lost City
679 Hydrothermal Field. *Science*, 319: 604-607.
680 Putnis, A., 1992. An introduction to mineral sciences. Cambridge University Press,
681 Cambridge, 457 pp.

682 Ramdohr, P., 1950. Über Josephinite, Awaruite, Souesite, ihre Eigenschaften,
683 Entstehung und Paragensis. *Mineralogical Magazine*, 29: 374-394.

684 Rimstidt, J.D., 1997. Quartz solubility at low temperatures. *Geochimica et*
685 *Cosmochimica Acta*, 61(13): 2553-2558.

686 Saccocia, P.J., Seewald, J.S., Shanks Iii, W.C., 2009. Oxygen and hydrogen isotope
687 fractionation in serpentine-water and talc-water systems from 250 to 450 °C,
688 50 MPa. *Geochimica et Cosmochimica Acta*, 73(22): 6789-6804.

689 Schandl, E.S., Naldrett, A.J., 1992. CO₂ metasomatism of serpentinites, south of
690 Timmins, Ontario. *Can. Mineral*, 30: 99-108.

691 Seewald, J.S., Zolotov, M.Y., McCollom, T., 2006. Experimental investigation of single
692 carbon compounds under hydrothermal conditions. *Geochim. Cosmochim.*
693 *Acta*, 70: 446-460.

694 Seyfried, W.E., Jr., Janecky, D.R., Berndt, M.E., 1987. Rocking autoclaves for
695 hydrothermal experiments. II. The flexible reaction cell system. In: Ulmer, G.,
696 Barnes, H. (Eds.), *Experimental Hydrothermal Techniques*. J. Wiley, N.Y., pp.
697 216-240.

698 Trommsdorff, V., Evans, B.W., 1977. Antigorite-ophicarbonates: Phase relations in a
699 portion of the system CaO-MgO-SiO₂-H₂O-CO₂. *Contributions to Mineralogy*
700 *and Petrology*, 60(1): 39-56.

701 Von Damm, K.L., 1995. Controls on the chemistry and temporal variability of
702 seafloor hydrothermal fluids. In: Humphris, S.E., Zierenberg, R.A., Mullineaux,
703 L.S., Thomson, R.E. (Eds.), *Seafloor Hydrothermal Systems: Physical,*
704 *Chemical, Biological and Geological Interactions*. AGU, Washington, D.C., pp.
705 222-247.

706 Weir, R.H., Kerrick, D.M., 1987. Mineralogic, fluid inclusion, and stable isotope
707 studies of several gold mines in the Mother Lode, Tuolumne and Mariposa
708 counties, California. *Economic Geology*, 82(2): 328-344.

709 Weiss, R.F., 1974. Carbon dioxide in water and seawater: the solubility of a non-ideal
710 gas. *Marine Chemistry*, 2(3): 203-215.

711 Whitmarsh, R.B., Manatschal, G., Minshull, T.A., 2001. Evolution of magma-poor
712 continental margins from rifting to seafloor spreading. *Nature*, 413(6852):
713 150-154.

714 Wolery, T.J., 1992. EQ3/6, A software package for geochemical modeling of aqueous
715 systems: Package overview and Installation guide (version 7.0). Lawrence
716 Livermore National Laboratory, Livermore, Ca.

717 Wolery, T.J., Jove-Colon, C.F., 2004. Qualification of Thermodynamic Data for
718 Geochemical Modeling of Mineral-Water Interactions in Dilute Systems.

719 Wolf, G.H., Chizmeshya, A.V.G., Diefenbacher, J., McKelvy, M.J., 2003. In Situ
720 Observation of CO₂ Sequestration Reactions Using a Novel Microreaction
721 System. *Environmental Science & Technology*, 38(3): 932-936.

722 Zhao, L., Sang, L., Chen, J., Ji, J., Teng, H.H., 2010. Aqueous carbonation of natural
723 brucite: relevance to CO₂ sequestration. *Environmental Science &*
724 *Technology*, 44(1): 406-411.

725

726